mathematics

MDPI

Article

Finite-Control-Set Model Predictive Control for Low-Voltage-Ride-Through Enhancement of PMSG Based Wind Energy Grid Connection Systems

Syed Wajahat Ali [1], Anant Kumar Verma [2], Yacine Terriche [3], Muhammad Sadiq [1], Chun-Lien Su [1,*], Chung-Hong Lee [1] and Mahmoud Elsisi [1,4]

[1] Electrical Engineering Department, National Kaohsiung University of Science and Technology, Kaohsiung City 807618, Taiwan
[2] Electric Power Conversion Systems Laboratory (SCoPE Lab), Universidad de O'Higgins, 611, Av. Libertador Bernardo O'Higgins, Rancagua 2820000, Chile
[3] Center for Research on Microgrids, Department of Energy Technology, Aalborg University, 9220 Aalborg, Denmark
[4] Department of Electrical Engineering, Faculty of Engineering at Shoubra, Benha University, Cairo 11629, Egypt
* Correspondence: cls@nkust.edu.tw

Abstract: Grid faults are found to be one of the major issues in renewable energy systems, particularly in wind energy conversion systems (WECS) connected to the grid via back-to-back (BTB) converters. Under such faulty grid conditions, the system requires an effective regulation of the active (P) and reactive (Q) power to accomplish low voltage ride through (LVRT) operation in accordance with the grid codes. In this paper, an improved finite-control-set model predictive control (FCS-MPC) scheme is proposed for a PMSG based WECS to achieve LVRT ability under symmetrical and asymmetrical grid faults, including mitigation of DC-link voltage fluctuation. With proposed predictive control, optimized switching states for cost function minimization with weighing factor (WF) selection guidelines are established for robust BTB converter control and reduced cross-coupling amid P and Q during transient conditions. Besides, grid voltage support is provided by grid side inverter control to inject reactive power during voltage dips. The effectiveness of the FCS-MPC method is compared with the conventional proportional-integral (PI) controller in case of symmetrical and asymmetrical grid faults. The simulation and experimental results endorse the superiority of the developed FCS-MPC scheme to diminish the fault effect quickly with lower overshoot and better damping performance than the traditional controller.

Keywords: model predictive control; PI control; wind energy; PMSG; reactive power; LVRT capability; grid faults

MSC: 93-08; 93B17; 93B35; 93B45; 93B51; 93B52; 93B70

Citation: Ali, S.W.; Verma, A.K.; Terriche, Y.; Sadiq, M.; Su, C.-L.; Lee, C.-H.; Elsisi, M. Finite-Control-Set Model Predictive Control for Low-Voltage-Ride-Through Enhancement of PMSG Based Wind Energy Grid Connection Systems. *Mathematics* **2022**, *10*, 4266. https://doi.org/10.3390/math10224266

Academic Editor: António Lopes

Received: 15 October 2022
Accepted: 10 November 2022
Published: 15 November 2022

1. Introduction

Recently, renewable energy sources like wind power farms are witnessing rapid incorporation into the electric power market, primarily because of reduced carbon footprint with less dependence on fossil fuels [1]. On the flip side, these sources are attributed to a weak dynamic system performance that yields power quality and stability issues [2,3]. Fast-paced research has been conducted to mitigate issues related to power control and grid faults by modifying the integration strategies in grid-connected wind turbines (GCWT) systems [4]. LVRT standards obligate a wind generation system to be linked to the power system during uncertain grid conditions and faults [5,6]. According to E.ON-Netz, Germany, LVRT condition requires an RES to retain grid connection and inject reactive power during grid irregularities [7]. Moreover, these issues motivate network authorities to revise

the grid codes to enforce LVRT as a key capability for stable and robust GCWT systems operation [8,9],

Control problems in GCWT systems are usually dealt with using vector control [10]. In such schemes, active and reactive power components are generated by decoupling the system current into rotating reference frame (dq-frame) currents. Conventionally, PI-based controllers regulate rotor current vectors through the machine side converter (MSC) as well as grid current vectors through the grid side converter (GSC) [11,12]. Due to intrinsic restrictions of the PI controllers, particularly with nonlinear systems and for better grid fault mitigation, various advanced control techniques as well as hardware solutions are presented in the literature [13–22].

A compound method having repetitive control and fuzzy based PI control is proposed in [13] for power smoothening in a PMSG based GCWT system. Likewise, better THD with enhanced LVRT ability is achieved in a grid connected WECS using adaptive parameter for a neural-fuzzy hybrid control [15]. Using a feedback linearizing scheme, a sliding mode control is exploited in [16] to mitigate the sub synchronous oscillations under various grid disturbances in the connected wind energy system. In [17], authors applied virtual synchronous machine (VSM) on a PMSG-based WT network to analyze the small signal stability of the proposed controllers. Nevertheless, most of these control schemes fall short when it comes to requirements such as abundant memory, model accuracy, computation time, and big data for an effective learning process.

Some hardware modifications approaches are used to enhance LVRT functionality in GCWT systems. To protect the BTB converter of GCWT against high rotor current in case of grid faults, a crowbar circuit is generally applied [17,18]. Likewise, more viable hardware option for enhanced LVRT capability is to link the energy storage systems (ESSs) with GSC of the GCWT system [20]. The ESS based system helps to store energy, while in the crowbar option, power dissipation is the only way out. An alternative method used for reactive power compensation and grid support at the PCC is to install flexible AC transmission systems (FACTS) devices, such as a dynamic voltage restorer (DVR) [21], the static synchronous compensator (STATCOM) [22], and static var compensator (SVC) [14]. Although these devices help to maintain constant voltage levels, nevertheless, the majority of such devices are not cost-effective and make the system more expensive and multifarious.

Underlying research on enhancing the LVRT capability of PMSG-based GCWT systems is subject to achieving objectives such as regulating the rotor overcurrent and DC-link overvoltage as well as controlling the active and reactive power under and during grid faults/voltage dips [23]. In such constrained problems, MPC proved to be a prime framework due to its recurrent optimization of control objectives over a receding horizon [24]. The prediction procedure occurs at each sample time to achieve cost function minimization. Error is generated by comparing the reference value with the measured output from the system, which acts as future information for the subsequent sample period for every variable. There are two broad categories of MPC discussed in the literature, namely continuous control set [25] and finite control set (FCS) [26]. When compared to continuous MPC, FSC-MPC has the advantage of processing the switching signals directly as control inputs, thus avoiding the need for a modulation stage. FCS-MPC is more appropriate for the applications relating to the control of power inverters [27].

On the other hand, there are some obstacles while using FCS-MPC for the GCWT systems. One major issue is the time-consuming computations while searching for the optimal or minimal values from all the possible switching state vectors. This exhaustive search limits controller computation ability as well as decreases the step length of the prediction horizon [28]. Another challenge is selecting the right weighting factors (WFs) for the cost function. Generally, high WF is assigned to the cost function term with higher error values. Typically, algorithms related to evolutionary search are used for WF determination. Several other schemes make use of dynamic WF gain as the error function to tune WF online [29,30]. Nonetheless, unsuitable WF selection may complicate the cost function,

worsening the overall control effort. Consequently, there is a trade-off amid accuracy and simplicity.

Keeping in mind the shortcomings mentioned in the literature above, this study proposes an improved FSC-MPC scheme to boost the de-coupled control of the injected real and reactive power into the power grid. With the suggested FCS-MPC scheme, both the machine side converter (MSC) and GSC of the GCWT system are controlled to suppress dc-link overvoltage and to meet LVRT demand using cost function minimization during transient conditions. The proposed scheme helps adjust the WFs only during transient or fault conditions while keeping a uniform value under steady-state condition for each coefficient of the cost function. Besides, Lyapunove's stability criteria as well as parameter sensitivity analysis are carried out to inspect the stability and robustness of the proposed control scheme. To summarize, the key aspects and contributions of this study are:

- An FCS-MPC scheme is utilized to enhance the LVRT operation of a PMSG-based grid connected wind generation system.
- Optimized switching states are selected by proposed predictive model to achieve reduced cross-coupling errors of active and reactive power predictions.
- Priority-based weighting factors are tuned for faster performance of the controller for P and Q power injection under various grid scenarios.
- DC-link overvoltage oscillation mitigation with better reference tracking.
- Lyapunove's stability criterion and parameter robustness analysis have been performed.
- Improved implementation of proposed scheme under both symmetrical and asymmetrical grid faults in accordance with recommended grid codes.
- Dynamic performance analysis and comparison of the proposed FCS-MPC method with classical PI controller.
- Experimental verification of the simulated results.

The remaining parts of the article are organized as follows. In Section 2, detailed time domain modelling of GCWT system is provided. The proposed FCS-MPC approach and its application on MSC and GSC is described in Section 3. Finally, Sections 4 and 5 present simulation as well as experimental results and conclusions, respectively.

2. Grid Connected Wind Turbine System

The design and modelling of PMSG based GCWT system is established in this section. Firstly, the mechanical specifics of the wind turbine are discussed, followed by the modeling of the B2B converter system, which entails MSC, GSC, DC-link, and the converter output filter, as shown in Figure 1.

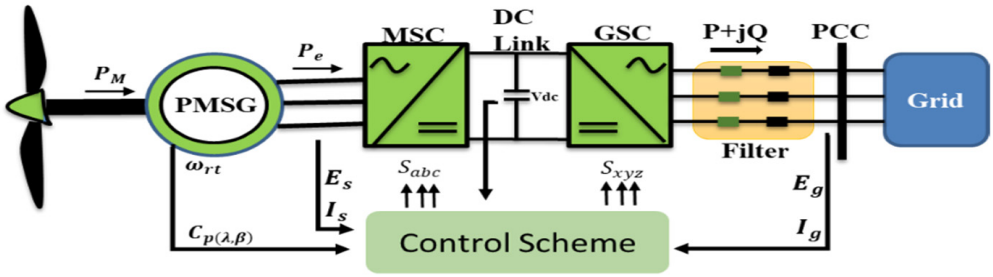

Figure 1. PMSG based GCWT System.

2.1. Wind-Turbine Modeling

The energy harnessed by the wind turbine is related to the wind speed and the turbine characteristics that can be expressed as [31]:

$$P_M = 0.5\left[\rho A C_{p(\lambda,\beta)} v^3\right] \quad (1)$$

where ρ is the density of the air, A is the swept area by the turbine blades, v is the speed of the wind, and C_p denotes the power coefficient, which is contingent upon tip speed ratio λ as well as pitch angle β. The value of λ is equated as

$$\lambda = \frac{\omega_{rt}\vartheta_{wb}}{v} \tag{2}$$

where ω_{rt} is the rotational speed of the turbine and ϑ_{wb} is the blade length of the wind turbine. Through the adjustment of λ, the maximum power can be extracted in case of varying the wind velocities with a maximum $C_{p(\lambda,\beta)}$ of 0.48 (Betz limit) at zero pitch angle as [31]:

$$C_{p(\lambda,\beta)} = 0.5175\left(-0.4\beta + \frac{116}{\lambda_a}\right)e^{\left(\frac{21}{\lambda_a}\right)} + \left(6.8e^{-3}\right)\lambda_a \tag{3}$$

where λ_a represents the constructional constraint constant.

2.2. Multiphase PMSG Modeling

The mathematical modeling of PMSG is mostly performed in space vector form by using park transformation. This transformation makes use of dq-frame or synchronous reference frame (SRF) to represent machine side variables such as voltages, power, and torque of the PMSG, as presented in Equations (4)–(8) [32]:

$$V_{ds} = -\omega_r L_s I_{qs} + RI_{ds} + L_s\frac{dI_{ds}}{dt} \tag{4}$$

$$V_{qs} = \omega_r L_s I_{ds} + \omega_r \Psi_r + RI_{qs} + L_s\frac{dI_{qs}}{dt} \tag{5}$$

$$T_{e.m} = \frac{3}{2}P\left[I_{qs}\Psi_r\right] \tag{6}$$

$$P_{stator} = \frac{3}{2}\left(V_{ds}I_{ds} + V_{qs}I_{qs}\right) \tag{7}$$

$$Q_{stator} = \frac{3}{2}\left(V_{qs}I_{ds} - V_{ds}I_{qs}\right) \tag{8}$$

where V_{ds}, V_{qs} are the stator voltages, I_{ds}, I_{qs} are the stator currents, L_s is the inductance of the stator, R is stator resistance, ω_r is the speed of the electric field, Ψ_r is the rotor flux linkage, $T_{e.m}$ is the electromagnetic torque, and P is the number of poles.

The mechanical and electrical torques can be related as follows:

$$P_m = \omega_r T_m; \quad \frac{d\omega_r}{dt} = \frac{1}{D}(T_e - T_m) - \frac{B}{D}\omega_r \tag{9}$$

where P_m is the mechanical power of the wind turbine, D is the inertia of the system and B is the friction-coefficient. Similarly, the mathematical model of GSC in dq-frame can be represented as follows [33]:

$$E_{dg} = V_{gd} - \omega_g L_g I_{qg} + R_g I_{dg} + L_g\frac{dI_{dg}}{dt} \tag{10}$$

$$E_{qg} = V_{gq} + \omega_g L_g I_{qg} + R_g I_{qg} + L_g\frac{dI_{qg}}{dt} \tag{11}$$

where E_{dg}, E_{qg} are the output inverter voltages, V_{gd}, V_{gq} are the grid voltages, I_{dg}, I_{qg} are the grid currents, L_s is the inductance of the filter, R_g is the filter resistance, and ω_g denotes the grid angular frequency.

3. FCS-MPC Scheme in Grid Connected Inverters

The FCS-MPC has become increasingly popular for the control and optimization of the grid-tied inverters [34]. The FCS-MPC is inherently a recurrent process at every sampling instant in order to determine the optimum future voltage vector of the inverter, which is close to the reference signal. In this way, those switching states, which minimize the cost function, are selected to be applied to the converter for the next sampling instant. The schematic of a grid-tied inverter is shown in Figure 2.

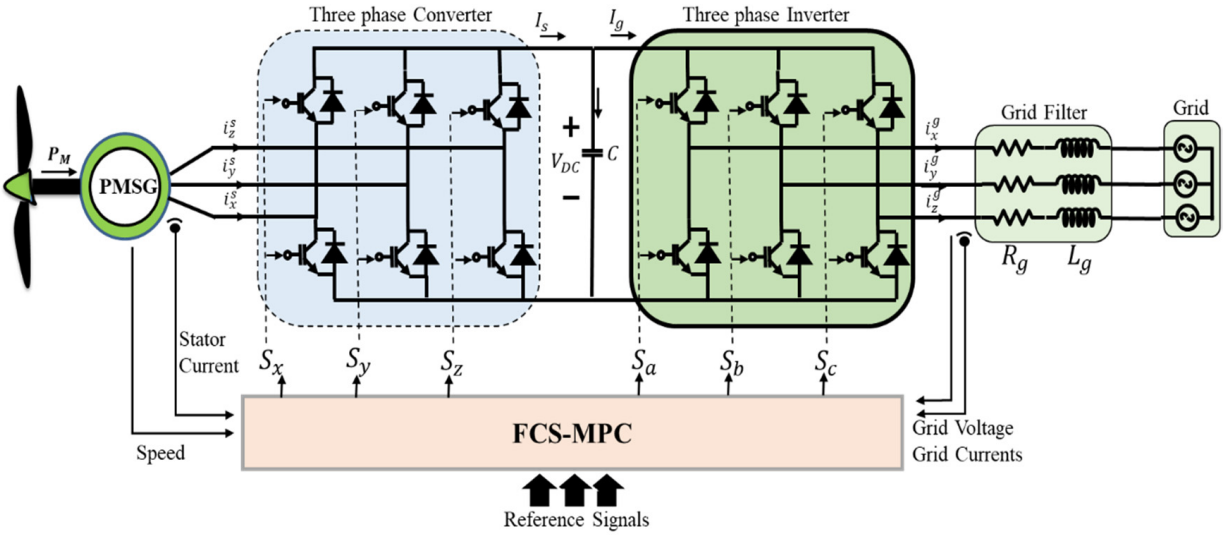

Figure 2. PMSG-based Grid-connected Inverter with FCS-MPC.

The switching states (Sx, Sy, Sz, Sa, Sb, Sc) have the following conditions:

$$S = \begin{cases} 0, & \text{switch in upper leg open, lower one closed} \\ 1, & \text{switch in upper leg close, lower one open} \end{cases} \tag{12}$$

The system dynamics at both sides of the DC-link capacitor can be written as follows:

$$\frac{d}{dt} v_{dc} = \frac{1}{C}(I_s - I_g) \tag{13}$$

$$I_s = \left(i^s_{xyz}\right)^T S_{xyz};\ i^s_{xyz} = \left(i^s_x\ i^s_y\ i^s_z\right)^T \tag{14}$$

$$I_g = \left(i^g_{xyz}\right)^T S_{abc};\ i^g_{xyz} = \left(i^g_x\ i^g_y\ i^g_z\right)^T \tag{15}$$

where v_{dc} is the DC-link voltage, I_s is stator current attained by the product of measured MSC currents (i^s_x, i^s_y, i^s_z) and switching states S_{abc}. Similarly, I_g is the grid current obtained by the product of measured GSC currents (i^g_x, i^g_y, i^g_z) and switching states S_{xyz}. Here, eight sequences of the switching state vectors are possible, either for MSC (S_{xyz}) or GSC (S_{abc}) sides. The finite switching states and corresponding voltage vector outputs on GSC are listed in Table 1.

Conventionally, the selection of switching states for the voltage vectors in a given cost function is subject to the lowest value by that particular state. However, this method is time-consuming, as all eight switching states need to be assessed through the cost function. In this study, we deal with the PMSG-based grid with faults, where control scheme is required to make quick decisions to comply with LVRT conditions. Therefore, to avoid the evaluation of each switching state in every cycle, evaluation is done when one of the switches changes its state as compared to the previous state. Hence, four out of eight possible states are checked in this case to reduce calculation complexity, as shown in Table 2.

Table 1. Operating and switching states.

State	Sa	Sb	Sc	Vector
0	0	0	0	0
1	1	0	0	V_{DC}
2	1	1	0	V_{DC}
3	0	1	0	V_{DC}
4	0	1	1	V_{DC}
5	0	1	1	V_{DC}
6	1	0	1	V_{DC}
7	1	1	1	0

Table 2. Subsequent probable states for the proposed controller scheme.

States	Existing States	Subsequent States (S_x S_y S_z)
0	(000)	(000) (001) (100) (010)
1	(100)	(000) (100) (101) (110)
2	(110)	(100) (010) (110) (111)
3	(010)	(000) (010) (011) (110)
4	(011)	(001) (010) (011) (111)
5	(001)	(000) (001) (011) (101)
6	(101)	(001) (100) (101) (111)
7	(111)	(101) (011) (110) (111)

For a non-zero voltage vector from the previous cycle, it will either maintain its state or switch to an adjacent vector. On the other hand, if the switching voltage vector from the previous cycle has a zero state, the resultant switching could be any nonzero vector. Figure 3 displays the switching sequence of the optimized voltage vectors.

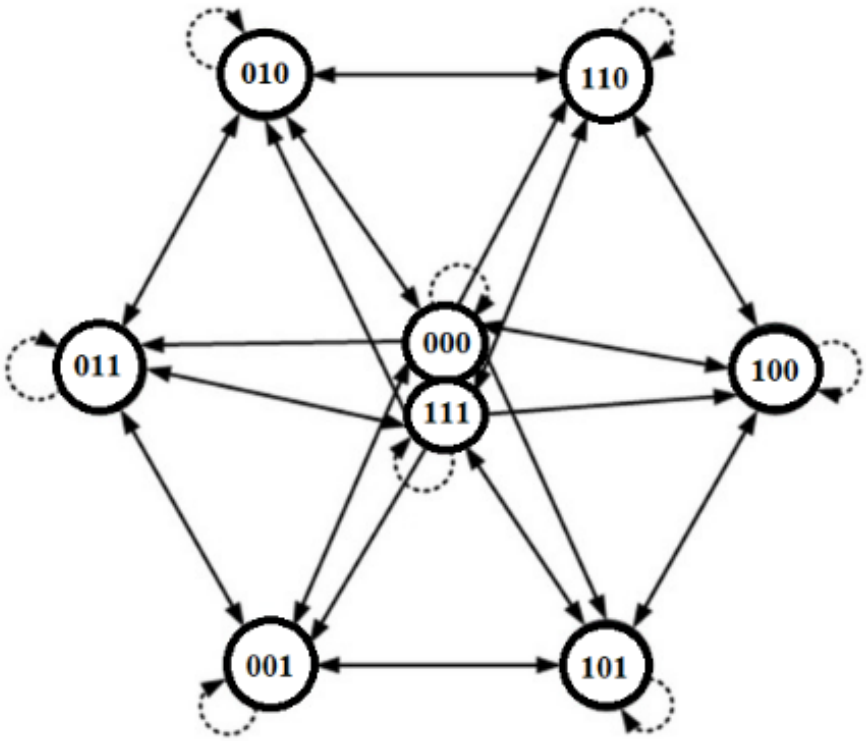

Figure 3. Selection of optimum switching vectors.

Under grid fault conditions, grid voltage drops instantly. As a result, the grid current rises to maintain the active power. When the grid voltage drops significantly, the current

injection will reach a maximum allowed value, which may eventually decrease active power transfer to the load. This imbalance between input and output power causes an upsurge in the DC-link voltage magnitude. To keep the magnitude of DC-link voltage stable and to achieve better LVRT ability, the proposed FCS-MPC scheme suggests the use of controlling dq-frame currents on both sides of the DC link capacitor. Note that an increased rotor speed happens as grid power demand reduces during fault. Thus, the increase in speed will be compensated with rotor inertia by retaining a constant DC link voltage. Eventually, to meet LVRT requirements, reactive power is provided to the grid, and the active power is reduced under faulty conditions.

3.1. Machine Side Converter (MSC) Control

The FCS-MPC control scheme for MSC is a discrete-time technique applied in sampled time intervals. There are eight possible switching states for inverter voltage vectors. As stated, out of the total eight voltage vectors, two are null vectors. Using Euler approximation, Equations (4) and (5) can be transformed into equivalent discrete-time predicted forms as follows:

$$I_{ds(k+1)} = \left(1 - \frac{t_{int}R}{L_s}\right) I_{ds(k)} + \frac{t_{int}}{L_s} V_{ds(k)} + \omega_r I_{qs(k)} t_{int} \tag{16}$$

$$I_{qs(k+1)} = \left(1 - \frac{t_{int}R}{L_s}\right) I_{qs(k)} + \frac{t_{int}}{L_s} V_{qs(k)} - \omega_r I_{ds(k)} t_{int} - \frac{t_{int}}{L_s} E_{s(k)} \tag{17}$$

where k is the sampling interval. Equations (16) and (17) represent future values of the stator current $I_{s(k+1)}$ in dq-frame while taking into consideration all possible voltage vectors $V_{s(k)}$ generated by MCS, the measured stator current $I_{s(k)}$, and the stator voltage, i.e., E_s.

In this work, the Euclidean norm is selected for cost function due to its better traceability property. The cost function takes into account the stator currents all in dq-frame as follows:

$$C_a = (I_{ds(k+1)} - I^*_{ds(k+1)})^2 + (I_{qs(k+1)} - I^*_{qs(k+1)})^2 + F_{MSC} \tag{18}$$

The first two terms in (18) are devoted to tracking the references, i.e., calculating the error between the reference and forecasted stator currents in the dq-frame, and F_{MSC} is a bounded non-linear function for stator current magnitude, which can be represented as follows:

$$F_{MSC} = \begin{cases} 0 \; for \; i_d < i_{s,M} \; and \; i_q < i_{s,M} \\ \infty \; for \; i_d > i_{s,M} \; or \; i_q > i_{s,M} \end{cases} \tag{19}$$

Equation (19) shows that the maximum allowed value of the stator current i.e., $i_{s,M}$, that corresponds to the voltage vector, chosen for cost function minimization. Conversely, the cost function C_a will become infinity for any voltage vector, which corresponds to a value of stator current greater than $i_{s,M}$. Using (6), the value of the q-axis stator current reference is expressed as (20), where the optimum torque is obtained from the MPPT speed control. Figure 4 illustrates the proposed FCS-MPC approach with an internal PI loop and external current feedback loop.

$$I^*_{qs} = \frac{2T_{e.ref}}{3P\Psi_r} \tag{20}$$

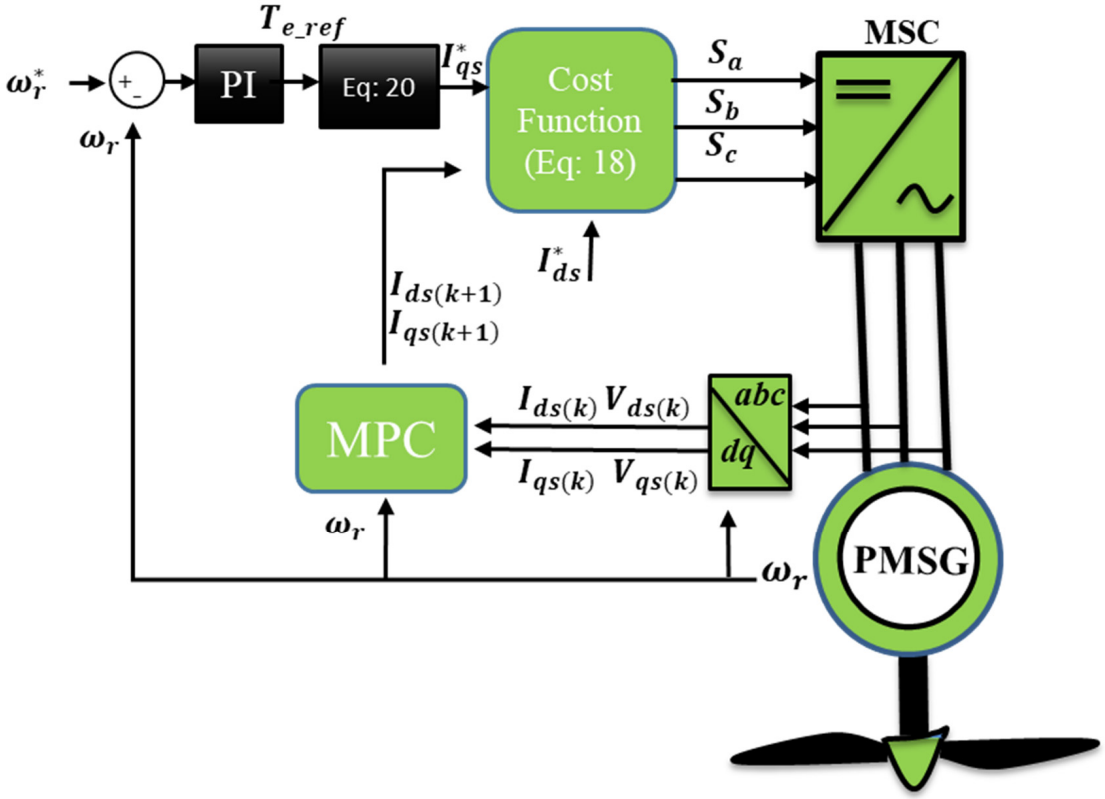

Figure 4. MSC with proposed FCS-MPC scheme.

3.2. Grid Side Converter (GSC) Control with FCS-MPC

Usually, GSC serves the purpose of stabilizing the DC-link voltage v_{dc} in case of faults or load variations on the grid side. The FCS-MPC controller in this study regulates the active and reactive power as well as DC link voltage by controlling d-axis and q-axis grid currents. Using (10) and (11), the discrete-time conversion of the dq-frame grid current is specified as follows [35].

$$\begin{bmatrix} I_{dg(k+1)} \\ I_{qg(k+1)} \end{bmatrix} = \Phi \begin{bmatrix} I_{dg(k)} \\ I_{qg(k)} \end{bmatrix} + \Gamma_i \begin{bmatrix} E_{dg(k+1)} \\ E_{qg(k+1)} \end{bmatrix} + \Gamma_g \begin{bmatrix} V_{gd(k)} \\ V_{gq(k)} \end{bmatrix} \tag{21}$$

where Φ, Γ_i, and Γ_g are the state matrices parameters in discrete time.

Using Langrage's extrapolation approach, k^{th} to $(k+1)^{th}$ instant generation of reference grid current is equated as follows:

$$\begin{cases} I^*_{dg(k+1)} = 4I^*_{dg(k)} - 6I^*_{dg(k-1)} + 4I^*_{dg(k-2)} - 4I^*_{dg(k-3)} \\ I^*_{qg(k+1)} = 4I^*_{qg(k)} - 6I^*_{qg(k-1)} + 4I^*_{qg(k-2)} - 4I^*_{qg(k-3)} \end{cases} \tag{22}$$

From the GSC predictive controller, the future values of the grid currents $I_{g(k+1)}$ are predicted for the given switching states using (23). Finally, from the cost function in (24), the error between the predicted and reference values of the grid currents becomes:

$$C_b = \gamma_d (I^*_{dg(k+1)} - I_{dg(k+1)})^2 + \gamma_q (I^*_{qg(k+1)} - I_{qg(k+1)})^2 \tag{23}$$

where γ_d and γ_q are dq-frame weighting elements of grid currents for frequency regulation. Active power minimization is achieved through the first term of (24), while reactive power

transfer to the grid is tracked by the second term. Active and reactive power to the grid is equated as follows:

$$\begin{cases} P_{g(k+1)} = 1.5\left(v_{dg(k+1)} I_{dg(k+1)}\right) \\ Q_{g(k+1)} = -1.5\left(v_{qg(k+1)} I_{qg(k+1)}\right) \end{cases} \quad (24)$$

As depicted in Figure 5, through the internal DC-link voltage control loop, the d-axis reference grid current $I^*_{dg(k+1)}$ is generated, which controls the active power transfer to the grid, while the reactive power is regulated by the q-axis grid current $I_{qg(k+1)}$, for which the reference can be obtained as:

$$I^*_{qg(k+1)} = \frac{Q_{g.ref(k)}}{-1.5 V_{gd(k+1)}} \quad (25)$$

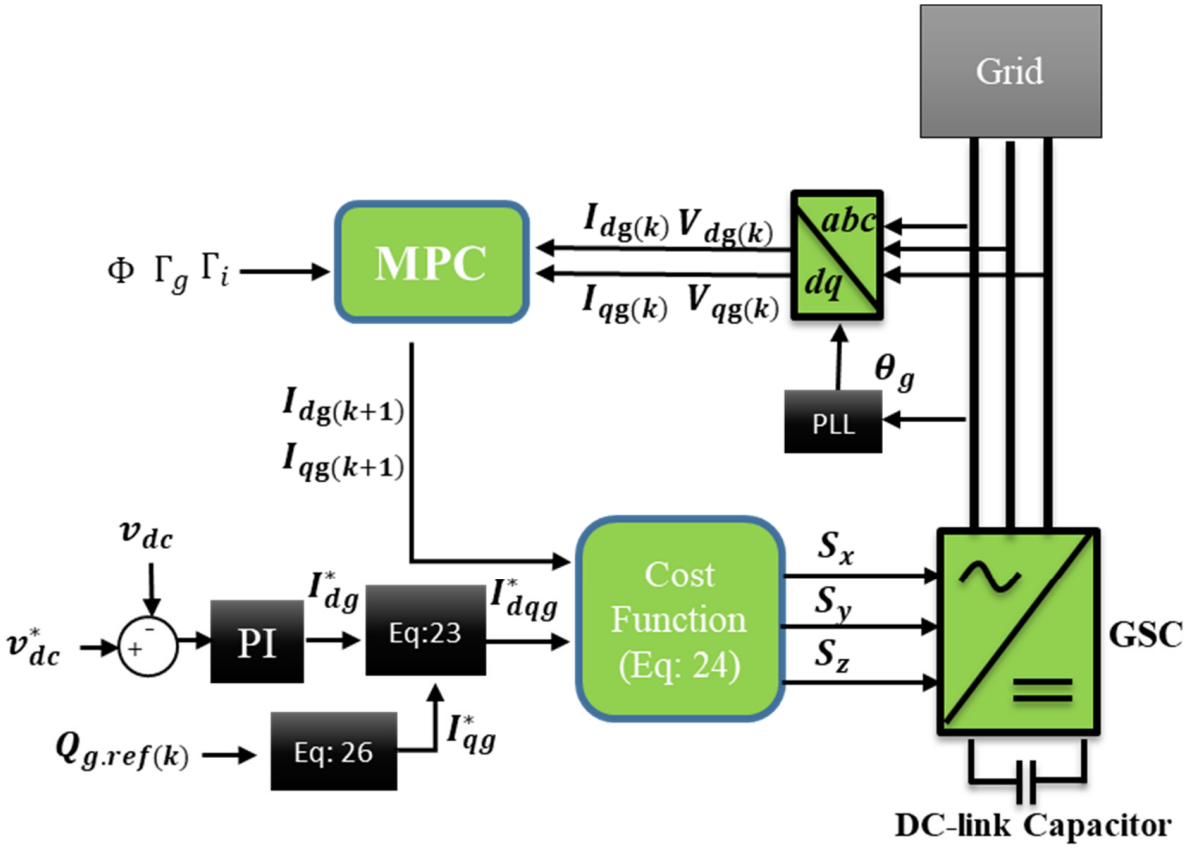

Figure 5. GSC with proposed FCS-MPC scheme.

3.3. Dynamic Weight Factors (γ_d, γ_q) Modification

The WFs in the cost function adjust the control objective to achieve an optimal output value. During steady state condition, a unity value is assigned to both the weights, as there is no change being detected. It is during the transient state when lower priority is granted to the term by dropping its weight factor, which is negatively affecting the cost function. This is further described in the flowchart in Figure 6, where a cross-coupling term is diminished by weight factor reduction.

Weight factors in the cost function are adjusted experimentally by iterative analysis and within the specified ranges in Table 3. For a sudden change in the active current with the constant reactive current (Sp < Sq), *Yd* is reduced to rectify the disturbance in the active power control, while *Yq* remains constant. Similarly, for an abrupt reactive power change (Sp > Sq), the penalty is now applied on *Yq* to reduce the cross-coupling effect and smoother operation.

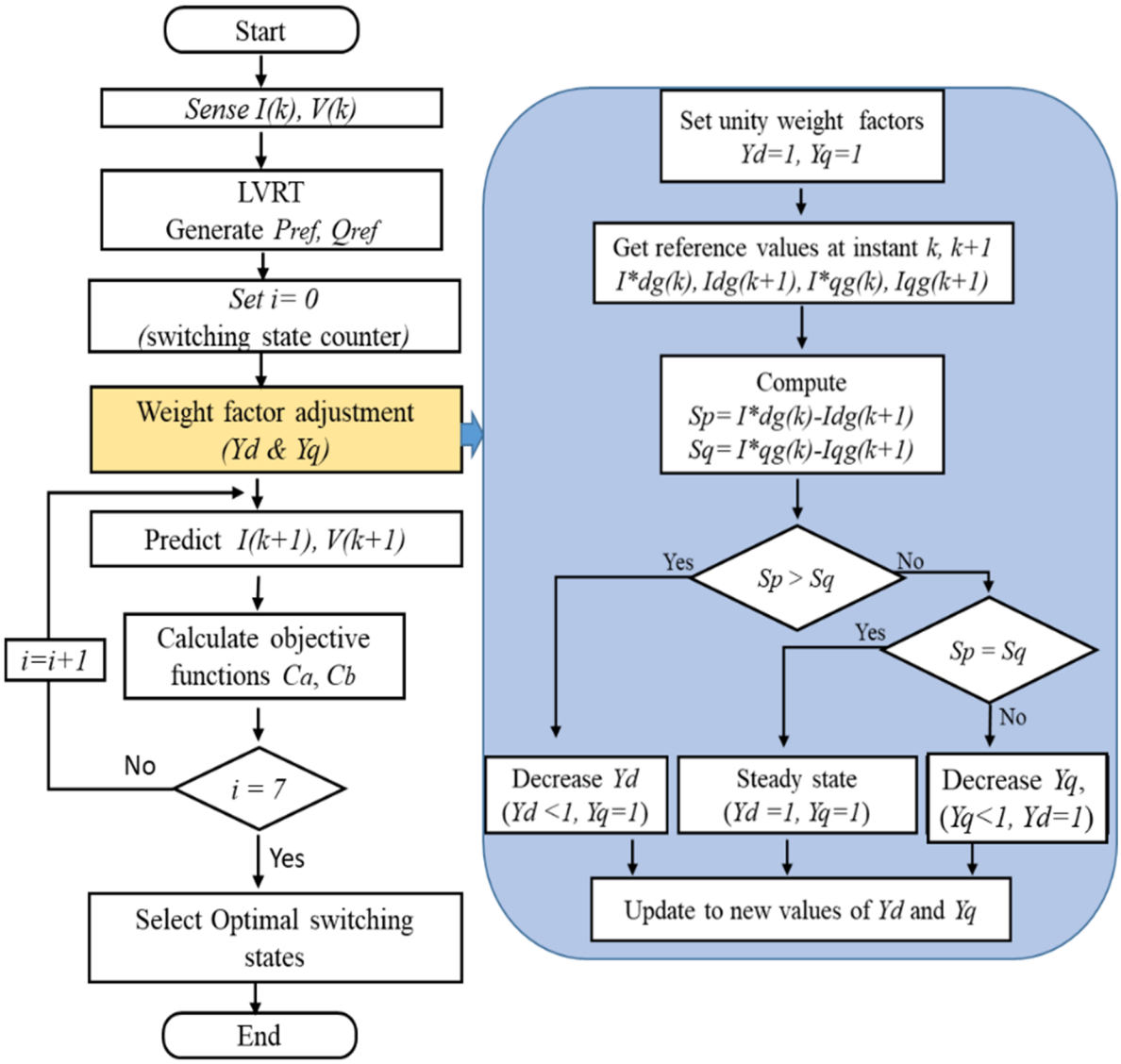

Figure 6. Flowchart of FCS-MPC with weight factor adjustment.

Table 3. WFs assortment criteria.

Parameter	Abrupt Active Power Change Sp < Sq	Steady-State Sp = Sq	Abrupt Reactive Power Change Sp > Sq
γ_d	(0.4–1)	1	1
γ_q	1	1	(0.2–0.8)

3.4. LVRT Requirements

One of the objectives of this study is to design the control scheme, which makes the GCWT system robust under symmetrical and asymmetrical voltage sags. To achieve this, the system needs to regulate the delivered active and reactive current injected into/absorbed from the power grid in accordance with grid integration standards and regulations [36]. The E.ON proposes that RES should supply 100% rated reactive current if a drop of 50% or more occurs in grid voltage for a predefined time duration [7].

With the occurrence of voltage sags, reactive power consumption/absorption by the grid is defined according to LVRT conditions as mentioned in grid codes [37]. In most cases, for a 50–90% drop in grid voltage magnitude, 2% reactive current of the total rated current

is needed for every 1% drop of the grid voltage. The overall reactive support in case of voltage dip on the grid is equated using Equation (26) as under [38]:

$$\begin{cases} Q_{g.ref} = 0 & \forall\ v_{grid} > 0.9v_n \\ Q_{g.ref} = (\frac{v_n - v_{grid}}{v_n})k & \forall\ 0.9v_n > v_{grid} > 0.5v_n \\ Q_{g.ref} = 1 & \forall\ v_{grid} < 0.5v_n \end{cases} \tag{26}$$

where v_n is nominal grid voltage, v_{grid} shows grid voltage in case of voltage dip, and k is the droop constant with its value not more than 2 [39]. The flow chart for the LVRT process is presented in Figure 7.

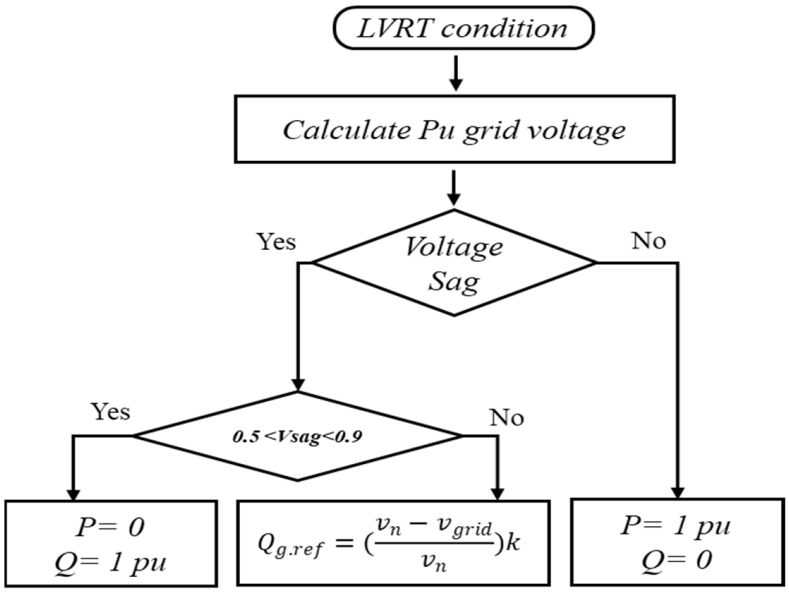

Figure 7. Flowchart of LVRT Scheme.

3.5. Stability Analysis

Lyapunav stability criterion is used to inspect the stability of the GCWT system in this study. Using (18), the error in the stator current can be collectively written as:

$$I_{s,err} = I_{S(k+1)} - I^*_{S(k+1)} \tag{27}$$

Using (16) and (17)

$$I_{s,err} = \left(1 - \frac{t_{int}R}{L_s}\right) I_{s(k)} + \frac{t_{int}}{L_s} V_{s(k)} - \omega_r I_{s(k)} t_{int} - \frac{t_{int}}{L_s} E_{s(k)} - I^*_{S(k+1)} \tag{28}$$

Here the control objective is to asymptotically minimize error $I_{s,err}$. The Lyapunove error function is written as

$$L(I_{s,err}) = \frac{1}{2}(I_{s,err})^2 \tag{29}$$

For a stable system, the derivative of Lyapunove function i.e., $\Delta L(I_{s,err})$, should be negative while $I_{s,err}$ converges to zero. Therefore, $I_{s,err}$ will lead to zero only if $\Delta L(I_{s,err}) < 0$. From (27), the time derivative of the Lyapunove function becomes:

$$\Delta L(I_{s,err}) = \frac{1}{2}\left[\left(1 - \frac{t_{int}R}{L_s}\right) I_{s(k)} + \frac{t_{int}}{L_s} V_{s(k)} - \omega_r I_{s(k)} t_{int} - \frac{t_{int}}{L_s} E_{s(k)}\right]^2 - \frac{1}{2}\left(I_{s,err(k)}\right)^2 \tag{30}$$

To ensure negative derivative of $\Delta L(I_{s,err})$, (4) in discrete form will be the future value of the voltage vector and can be written as:

$$V_s = -\omega_r \frac{L_s}{t_{int}} I_{s(k+1)} + E_{s(k)} + \frac{L_s}{t_{int}} L_{s(k)} \tag{31}$$

The criteria to be met by the system for Lyapunove stability is:

$$L\left(I_{s,err(k)}\right) \geq D_1 \left|I_{s,err(k)}\right|^{\beth}, \ \forall I_{s,err(k)} \in \Upsilon$$

$$L\left(I_{s,err(k)}\right) \geq D_2 \left|I_{s,err(k)}\right|^{\delta}, \ \forall I_{s,err(k)} \in \Gamma$$

$$L\left(I_{s,err(k+1)}\right) - L\left(I_{s,err(k)}\right) < -D_3 \left|I_{s,err(k)}\right|^{\delta} + D_4$$

$$D_1, \ D_2, \ D_3, \ D_4 \in \mathbb{R}^+, \ \delta \geq 1, \ \Upsilon \in \mathbb{R}^+, \ \Gamma \subset \Upsilon \tag{32}$$

Substituting (31) into (30), we get

$$\frac{1}{2}\left(\frac{t_{int}}{Ls}\right)^2 l^2 - \frac{1}{2}\left(I_{s(k)}\right)^2 \geq \Delta L_{(k)} \tag{33}$$

where $l \in \mathbb{R}^+$ is the quantization error. Using (32),

$$D_1 = D_2 = 1, \ D_3 = 0.5, \ D_4 = \frac{1}{2}\left(\frac{t_{int}}{Ls}\right)^2 l^2$$

Consequently, controlled parameters are limited within the bounded region, which is in accordance with Lyapunove stability criteria.

4. Simulation Results and Discussions

To monitor and evaluate the performance of the suggested FCS-MPC strategy, the following two scenarios are considered and performed in MATLAB/Simulink environment.

(a) P and Q transient performance with fixed and variable WFs.
(b) LVRT performance under symmetrical and asymmetrical faults on the grid.

In addition, comparisons are drawn between the proposed controller strategy and the PI controller to assess the operational performance during LVRT operations for the WECS [40]. The aforementioned control scheme is implemented by decoupling the d- and q-axes currents by using two PI controllers with feed-forward paths. In both loops, the PI controllers are tuned by plotting Bode plots of the open-loop transfer functions. To achieve critical damping behavior, the proportional gain has been set to get the frequency crossover in safe a margin, while integral gain has been set to get the highest gain without overshoots. The specification of the GCWT system is given in Table 4.

Table 4. Parameters of the GCWT system.

Parameter	Value
Rated Power	1.50 MW
Grid Voltage	576 V
DC link voltage	1150 V
Stator Resistor	3.2 mΩ
Stator Resistor	3.05 mH
Switching Frequency	20 KHz
DC-Link Capacitor	0.025 F
Filter Resistor	3.154 mΩ
Filter Inductor	0.44 mH

4.1. Analysis of Step-Change in Power (Active/Reactive)

The transient response of the FCS-MPC scheme is explored for different WFs operating conditions.

(a) Step-change in Active Power (P_{ref})

In this scenario, the decoupling ability is investigated with WFs fixed at unity, with a step change of 0 to 1 MW in reference active power P_{ref}, whereas the reactive power reference Q_{ref} is fixed at zero. During the transient period, the Q component experienced an unwanted cross-coupling in the case of fixed WFs. The cross-coupling on Q sustains for around 2.3 s, as shown in Figure 8a.

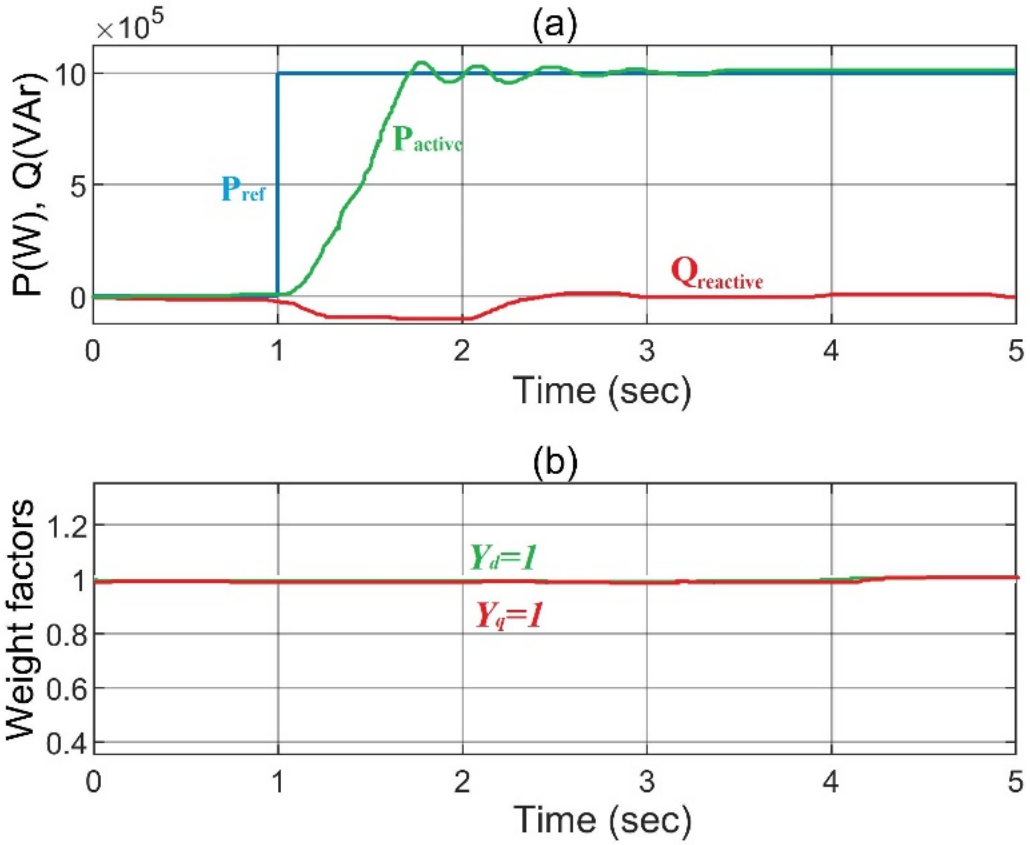

Figure 8. Step-response of FCS-MPC during fixed WFs. (**a**) Active power and Reactive power (**b**) Dynamics of WFs.

With variable WFs applied, the proposed FCS-MPC scheme successfully eliminates cross-couplings and reduces disturbances to insignificant values throughout the transient phase, as depicted in Figure 9a. Figure 8b illustrates the case of fixed WFs with unity value, while in the case of variable WFs, the *Yd* (as shown in Figure 9b) is adjusted, agreeing with the adjustment rule described in Table 3.

(b) Step-change in Reactive Power (Q_{ref})

In this section, the FCS-MPC transient performance is examined in an alternative operating scenario, where Q_{ref} is suddenly changed from 0–1 MVAr, while keeping P_{ref} at zero. Transient responses were examined with fixed and variable WFs, and the results are presented in Figures 10 and 11, respectively. FCS-MPC systems with variable WFs experienced a settling time of around 0.4 s, which is less than the case of fixed WFs systems, where it is around 0.9 s.

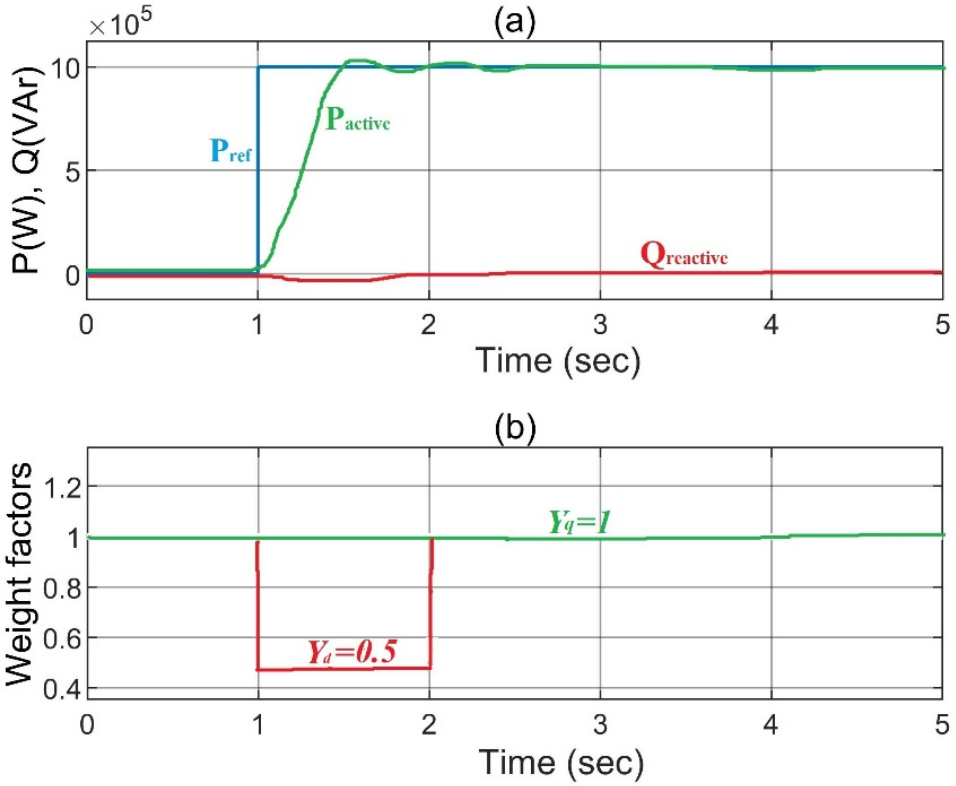

Figure 9. Step-response of FCS-MPC during Variable WFs. (**a**) Active power and Reactive power (**b**) Dynamics of WFs.

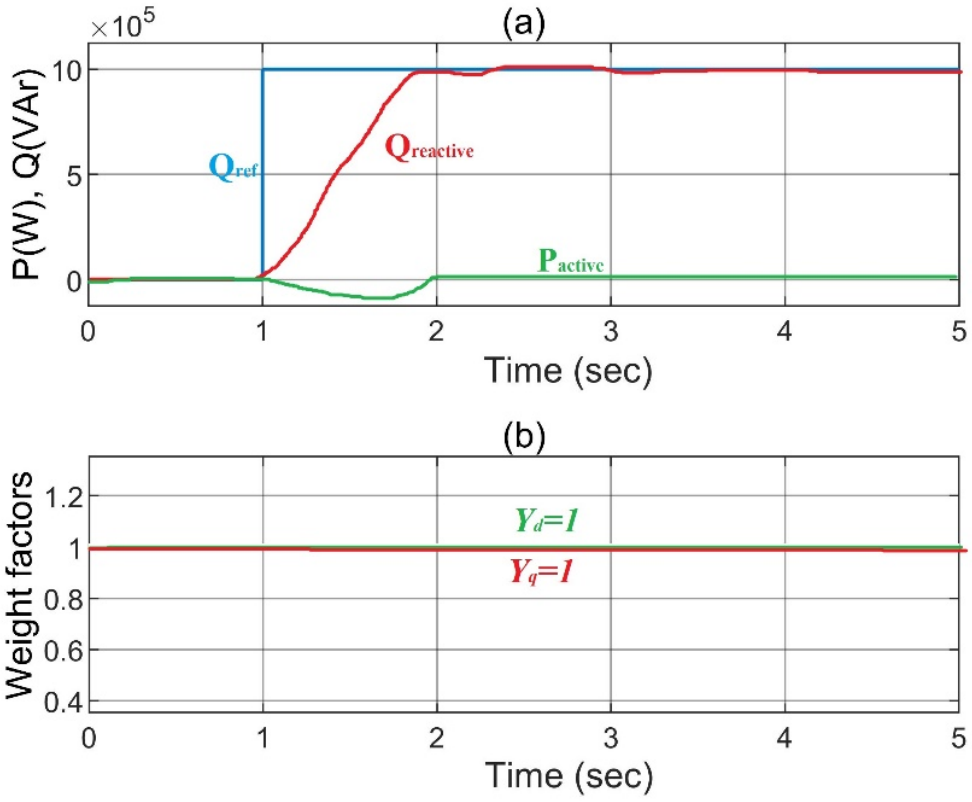

Figure 10. Step-response of FCS-MPC during fixed WFs. (**a**) Active power and Reactive power (**b**) Dynamics of WFs.

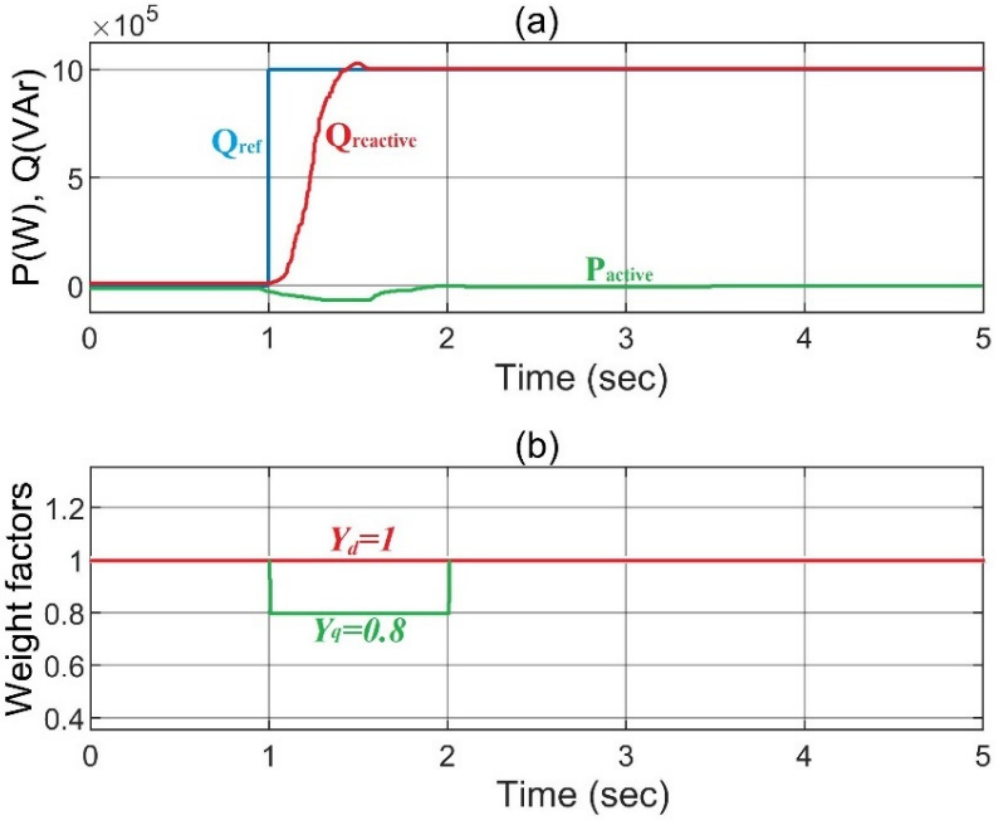

Figure 11. Step response of FCS-MPC during variable WFs. (**a**) Active and Reactive power (**b**) Dynamics of WFs.

In the findings illustrated in Figure 11a, the proposed FCS-MPC scheme with variable WFs, the cross-coupling is alleviated to a negligible level, and the disturbance is effectively mitigated during the transient phase. In this case, the value of *Yq* is regulated at 0.8.

4.2. Fault Analysis on the Grid Side

(a) Symmetrical Fault Analysis

Symmetrical voltage fault of 30% (0.3 p.u.) of grid voltage is introduced for 0.5 seconds i.e., from t = 2.5 s to t = 3 s, as presented in Figure 12. The three-phase grid voltage and resulting grid current waveforms during grid voltage sag are depicted in Figure 12a. During nominal grid conditions before the 3-phase fault, the active power is generated at 1 p.u., while no reactive power injection is done from the PMSG by keeping $i_{qg,ref}$ at zero. As the voltage dip occurs at the PCC, Figure 12b shows that the DC-link voltage is regulated at the reference value of 1150 V by virtue of the proposed MPC scheme. During the voltage dip on the grid, the active power reduces in relation to the voltage drop, as a mismatch of mechanical generated power and electrical supplied power happens. Figure 12d depicts the reactive power injection to support the grid in accordance with (27), as active power decreases during fault. Execution of this limitation scheme provides the supplementary capacity to GSC for reactive power injection for grid code compliance. The proposed MSC controller in this case regulates the generator speed so that it keeps the value of DC-link voltage near the reference value. Moreover, the system inertia takes care of the power mismatch with increased mechanical speed as shown in Figure 13.

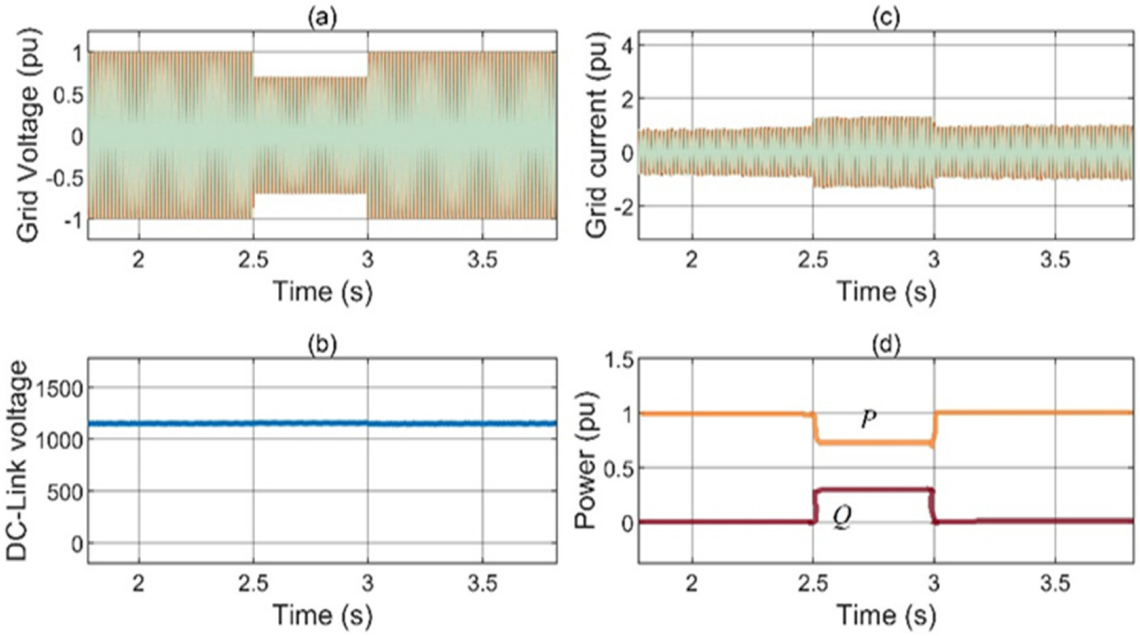

Figure 12. LVRT Performance of proposed scheme during symmetrical grid fault. (**a**) Grid voltage (**b**) Inverter current (**c**) DC-link voltage (**d**) Active and Reactive power.

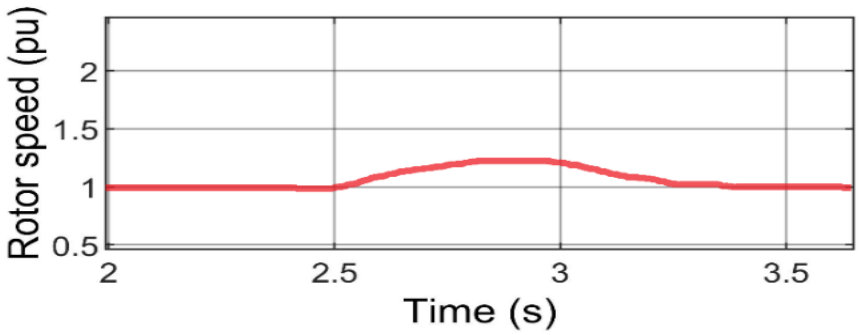

Figure 13. Increased rotor speed during fault.

In comparison to FCS-MPC, the conventional PI control method does not exhibit a satisfactory transient response, with the DC-link voltage ripple reaching 1490 V, as depicted in Figure 14b. Moreover, the PI controller fails to ensure optimum reactive compensation, with added delay to reach the steady-state value after the fault clears (Figure 14d).

(b) Asymmetrical Fault Analysis

The time and severity of the asymmetrical fault remained similar to the previous case. In the case of asymmetrical faults on the grid, a performance comparison of the proposed MPC controller is examined, as shown in Figure 15. Note that DC-link voltage remained stable with reduced fluctuations as shown in Figure 15b. The proposed controller is faster than the PI scheme in providing reactive power compensation is supplied to the grid as active power decreases with increased grid current due to the faulty condition.

With the PI methodology, in addition to DC-link voltage overshoot, the active power fluctuation with almost double the grid frequency is apparent in Figure 16d. Although GSC regulates the active and reactive power, the second-order DC-link oscillations adversely affect the converter operation. The settling time of the PI regulator is inferior, as it takes more time to achieve steady state as compared to the proposed predictive control scheme. This shows that the PI controller cannot deliver reasonable performance, indicating that the proposed MPC approach offers better LVRT performance.

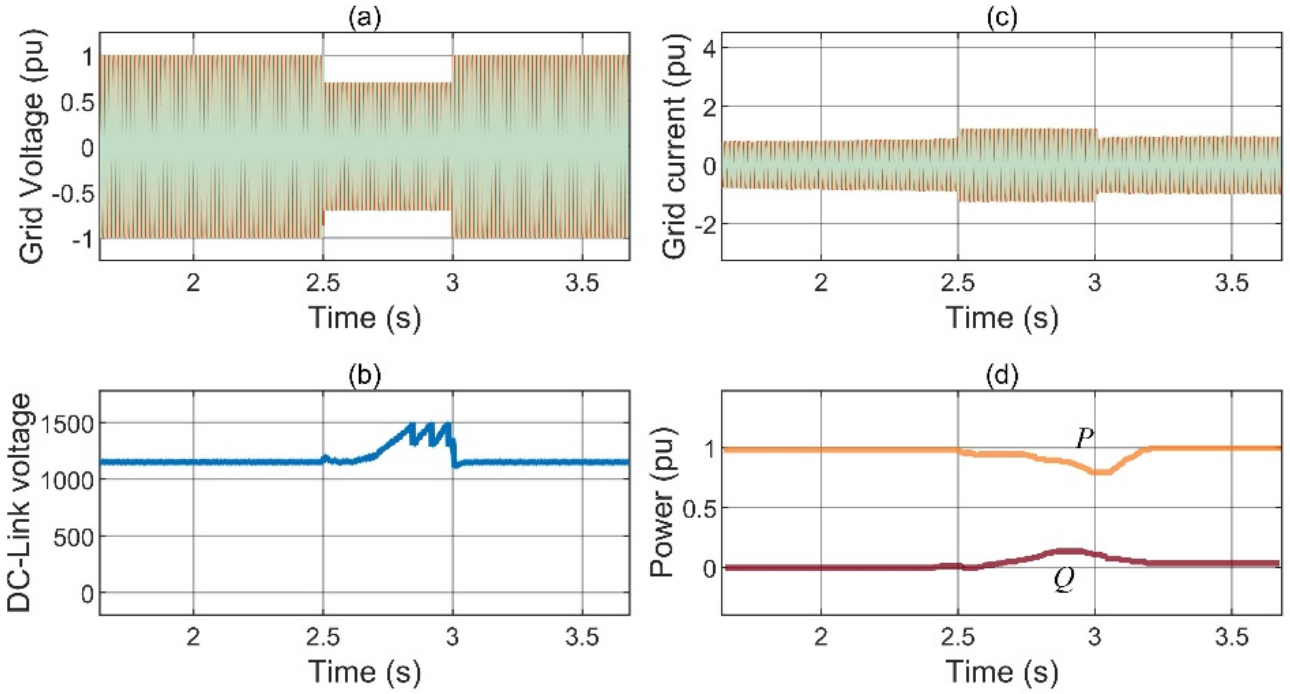

Figure 14. LVRT Performance of PI controller during symmetrical grid fault. (**a**) Grid voltage (**b**) Inverter current (**c**) DC-link voltage (**d**) Active and Reactive power.

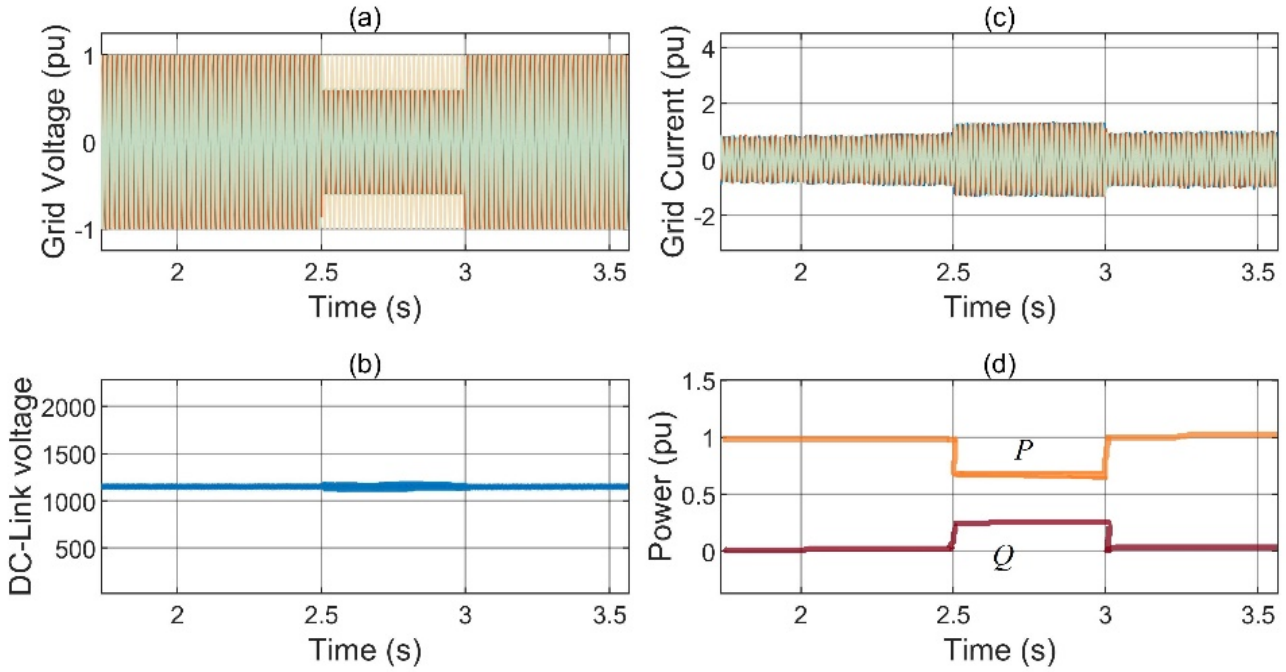

Figure 15. Enhanced LVRT capability of the proposed MPC scheme during asymmetrical grid faults. (**a**) Grid voltage (**b**) Inverter current (**c**) DC-link voltage (**d**) Active and Reactive power.

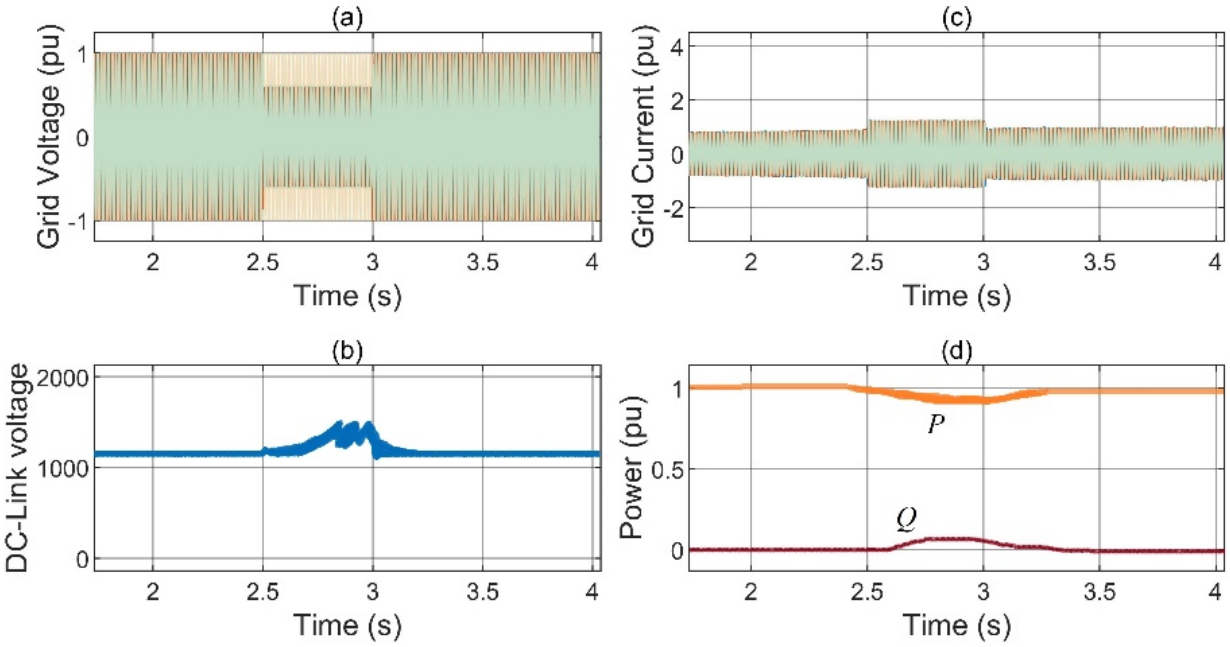

Figure 16. LVRT Performance of PI controller during asymmetrical grid fault. (**a**) Grid voltage (**b**) Inverter current (**c**) DC-link voltage (**d**) Active and Reactive power.

4.3. Experimental Results

In order to validate the performance of the proposed controller, an experimental setup is used as shown in Figure 17. The experimental verification is realized by OPAL-RT (OP5700) platform. The parameters of experimental tests are similar to those of simulation results. The sampling frequency of the FCS-MPC algorithm is 20 kHz, while the data sampling frequency is either 16 or 20 kHz, contingent upon the data logging duration as well as memory constraints.

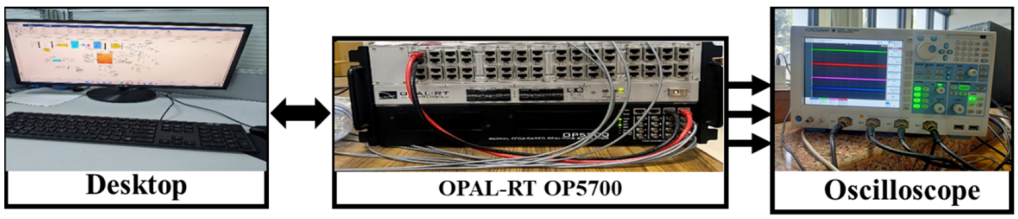

Figure 17. Experimental Steup.

Similar to simulation results, a symmetrical voltage sag of 30% is introduced at the grid side. As a result, dip in the grid voltage is evident, along with rise in inverter current in Figure 18. Furthermore, net DC-link voltage is upheld within at the reference value with very low ripple oscillations under sag conditions, as depicted in Figure 19.

The active and the reactive power are being regulated, corresponding to LVRT operation conditions. The dynamic response of the proposed predictive control is efficient in providing grid support by increasing in the reactive power injection along with active power reduction as the grid fault occurs. Thus, the results of the experimental setup presented here approve that the enhanced LVRT compliance can be achieved robustly by using the proposed FSC-MPC scheme.

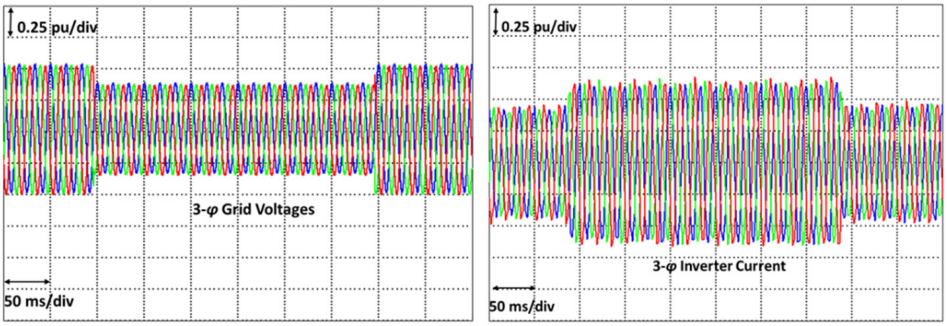

Figure 18. Grid Voltages and Inverter current under Symmetrical grid fault.

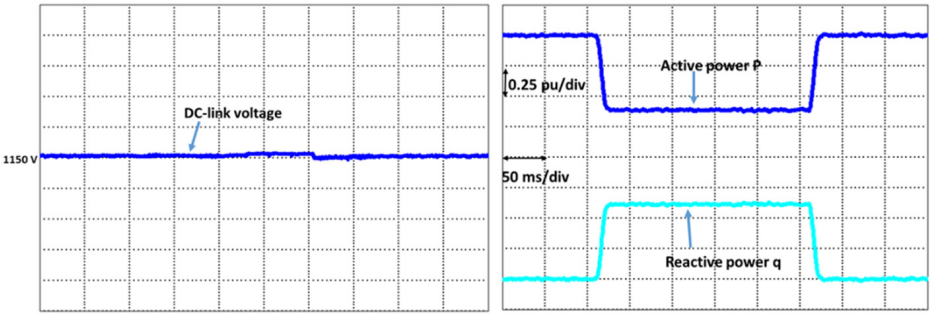

Figure 19. DC-link voLtage and Power regulation.

4.4. Parameter Robustness Analysis

With FCS-MPC being a model-based method, adequate system parameter values are pivotal for an overall robust control. Thus, the variation in the values of PMSG's resistance and inductance (L_s) do have a direct or indirect effect on the system performance, as can be seen from (16) and (17). The detuned PMSG model is used to examine the parameter robustness and sensitivity by variation in the values of L_s. The sensitivity of the proposed strategy is investigated by changing the L_s from 50% to 150% of its measured value. From Figure 20, it can be seen that dq-frame stator currents have higher oscillations in case of detuned parameter conditions as compared to real values. Nevertheless, the proposed FCS-MPC applied on the MSC side still manages to track the reference value under varying L_s conditions. The value of the stator current THDs in case of generator inductance variations of 50% and 150% are 7.35% and 8.81% respectively. Finally, a comparison of the proposed FCS-MPC and PI control with respect to parameter tuning, complexity, response, and computation cost/burden is summarized in Table 5. The computation burden here is the measure of execution time for the two control schemes. The execution time for the proposed scheme is longer than the simulation time, as FCS-MPC is required to execute at least three cycles to compute the predicted voltage vector values.

Table 5. Comparison of FCS-MPC and classical PI controller.

Features	PI Controller	FCS MPC
Parameter Decoupling	External	Internal
Tuning	Retuning required	Easy, no retuning needed
Secondary axis current control	Additional PI regulators required	Single cost function for error mitigation
Dynamic response	Slow	Fast
Computation burden	Medium	High

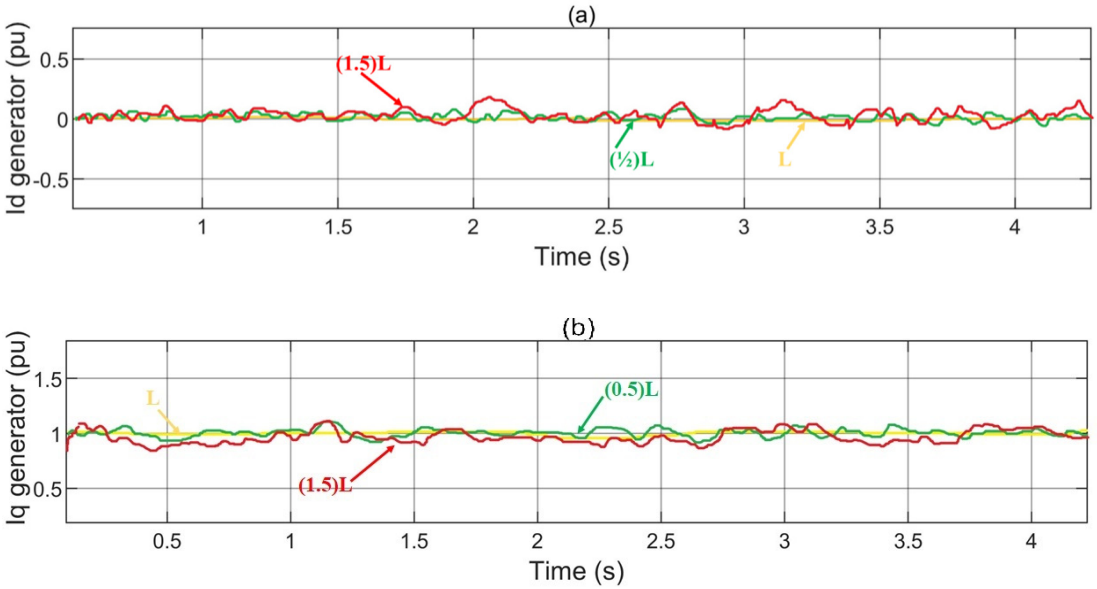

Figure 20. Parameter robustness analysis under inductance variation (**a**) d-axis stator current (**b**) q-axis stator current.

5. Conclusions

In this paper, time domain modeling and analysis of a direct-drive PMSG-based wind turbine along with FCS-MPC scheme with improved LVRT performances have been presented. In GCWT systems, the issues of cross-coupling of the active and reactive power during transient states have been addressed by efficiently incorporating variable WFs with the FCS-MPC scheme. The performance of the proposed controller is analyzed by fast selection and application of switching states on the MSC and GSC inverters during symmetrical and asymmetrical grid faults. Moreover, the abrupt increase in DC-link voltage in case of voltage dips is regulated using excess active power in rotor inertia of PMSG-based wind turbine during the faulty condition. The suggested FCS-MPC scheme shows better LVRT capability in comparison with the conventional PI control approach with enhanced DC-link voltage stability and reactive power compensation during various fault conditions.

Author Contributions: S.W.A.: investigation, conceptualization, methodology, software, writing—original draft; A.K.V.: conceptualization, methodology, validation; Y.T.: writing—review and editing; M.S.: data curation, conceptualization; C.-L.S.: supervision, writing—review and editing; M.E.: methodology, writing—review and editing; C.-H.L.: writing—review and editing. All authors have read and agreed to the published version of the manuscript.

Funding: The works of Chun-Lien Su and Mahmoud Elsisi were funded by the Ministry of Science and Technology of Taiwan under grant MOST 110-2221-E- 992-044-MY3 and MOST 110-2222-E-011-013.

Institutional Review Board Statement: Not applicable.

Informed Consent Statement: Not applicable.

Data Availability Statement: Not applicable.

Conflicts of Interest: The authors declare no conflict of interest.

References

1. Noman, F.M.; Alkawsi, G.A.; Abbas, D.; Alkahtani, A.A.; Tiong, S.K.; Ekanayake, J. Comprehensive Review of Wind Energy in Malaysia: Past, Present, and Future Research Trends. *IEEE Access* **2020**, *8*, 124526–124543. [CrossRef]
2. Bajaj, M.; Singh, A.K. Grid Integrated Renewable DG Systems: A Review of Power Quality Challenges and State-of-the-Art Mitigation Techniques. *Int. J. Energy Res.* **2020**, *44*, 26–69. [CrossRef]

3. Ali, S.W.; Sadiq, M.; Terriche, Y.; Naqvi, S.A.R.; Hoang, L.Q.N.; Mutarraf, M.U.; Hassan, M.A.; Yang, G.; Su, C.L.; Guerrero, J.M. Offshore Wind Farm-Grid Integration: A Review on Infrastructure, Challenges, and Grid Solutions. *IEEE Access* **2021**, *9*, 102811–102827. [CrossRef]
4. Xie, Q.; Zheng, Z.; Huang, C.; Dai, T. Coordinated Fault Ride Through Method for PMSG-Based Wind Turbine Using SFCL and Modified Control Strategy. *IEEE Trans. Appl. Supercond.* **2021**, *31*, 1–5. [CrossRef]
5. Mahela, O.P.; Gupta, N.; Khosravy, M.; Patel, N. Comprehensive Overview of Low Voltage Ride through Methods of Grid Integrated Wind Generator. *IEEE Access* **2019**, *7*, 99299–99326. [CrossRef]
6. Shi, K.; Song, W.; Xu, P.; Liu, R.; Fang, Z.; Ji, Y. Low-Voltage Ride-Through Control Strategy for a Virtual Synchronous Generator Based on Smooth Switching. *IEEE Access* **2017**, *6*, 2703–2711. [CrossRef]
7. E.ON2006-Netz-Grid Code-High and Extra High Voltage. Available online: https://wenku.baidu.com/view/6289c22bcfc789eb172dc88e.html (accessed on 6 October 2022).
8. Cardenas, R.; Pena, R.; Alepuz, S.; Asher, G. Overview of Control Systems for the Operation of DFIGs in Wind Energy Applications. *IEEE Trans. Ind. Electron.* **2013**, *60*, 2776–2798. [CrossRef]
9. Yujun, L.; Yuan, X.; Li, J.; Xu, Z. Novel Grid-Forming Control of Permanent Magnet Synchronous Generator-Based Wind Turbine for Integrating Weak AC Grid without Sacrificing Maximum Power Point Tracking Demand as Frequency Controlled Reserve View Project Stability Analysis and Control Scheme. *IET Gener. Transm. Distrib.* **2021**, *15*, 1613–1625. [CrossRef]
10. Benbouhenni, H.; Bizon, N. Advanced Direct Vector Control Method for Optimizing the Operation of a Double-Powered Induction Generator-Based Dual-Rotor Wind Turbine System. *Mathematics* **2021**, *9*, 2403. [CrossRef]
11. Qais, M.H.; Hasanien, H.M.; Alghuwainem, S. Optimal Transient Search Algorithm-Based PI Controllers for Enhancing Low Voltage Ride-Through Ability of Grid-Linked PMSG-Based Wind Turbine. *Electronics* **2020**, *9*, 1807. [CrossRef]
12. Yuan, L.; Meng, K.; Huang, J.; Dong, Z.Y. Investigating Subsynchronous Oscillations Caused by Interactions between PMSG-Based Wind Farms and Weak AC Systems. *Int. J. Electr. Power Energy Syst.* **2020**, *115*, 105477. [CrossRef]
13. Pan, L.; Wang, X. Variable Pitch Control on Direct-Driven PMSG for Offshore Wind Turbine Using Repetitive-TS Fuzzy PID Control. *Renew. Energy* **2020**, *159*, 221–237. [CrossRef]
14. Kapetanaki, A.; Levi, V.; Buhari, M.; Schachter, J.A. Maximization of Wind Energy Utilization Through Corrective Scheduling and FACTS Deployment. *IEEE Trans. Power Syst.* **2017**, *32*, 4764–4773. [CrossRef]
15. Manohar, G.; Venkateshwarlu, S.; JayaLaxmi, A. An Elite Approach for Enhancement of LVRT in Doubly Fed Induction Generator (DFIG)-Based Wind Energy Conversion System (WECS): A FAMSANFIS Approach. *Soft Comput.* **2022**, *26*, 11315–11337. [CrossRef]
16. Li, P.; Xiong, L.; Wu, F.; Ma, M.; Wang, J. Sliding Mode Controller Based on Feedback Linearization for Damping of Sub-Synchronous Control Interaction in DFIG-Based Wind Power Plants. *Int. J. Electr. Power Energy Syst.* **2019**, *107*, 239–250. [CrossRef]
17. Muftau, B.; Fazeli, M.; Egwebe, A. Stability Analysis of a PMSG Based Virtual Synchronous Machine. *Electr. Power Syst. Res.* **2020**, *180*, 106170. [CrossRef]
18. Haidar, A.M.A.; Muttaqi, K.M.; Hagh, M.T. A Coordinated Control Approach for DC Link and Rotor Crowbars to Improve Fault Ride-through of Dfig-Based Wind Turbine. *IEEE Trans. Ind. Appl.* **2017**, *53*, 4073–4086. [CrossRef]
19. Gebru, F.M.; Khan, B.; Alhelou, H.H. Analyzing Low Voltage Ride through Capability of Doubly Fed Induction Generator Based Wind Turbine. *Comput. Electr. Eng.* **2020**, *86*, 106727. [CrossRef]
20. Yan, L.; Chen, X.; Zhou, X.; Sun, H.; Jiang, L. Perturbation Compensation-Based Non-Linear Adaptive Control of ESS-DVR for the LVRT Capability Improvement of Wind Farms. *IET Renew. Power Gener.* **2018**, *12*, 1500–1507. [CrossRef]
21. Chawda, G.S.; Shaik, A.G.; Mahela, O.P.; Padmanaban, S.; Holm-Nielsen, J.B. Comprehensive Review of Distributed FACTS Control Algorithms for Power Quality Enhancement in Utility Grid with Renewable Energy Penetration. *IEEE Access* **2020**, *8*, 107614–107634. [CrossRef]
22. Sayahi, K.; Kadri, A.; Bacha, F.; Marzougui, H. Implementation of a D-STATCOM Control Strategy Based on Direct Power Control Method for Grid Connected Wind Turbine. *Int. J. Electr. Power Energy Syst.* **2020**, *121*, 106105. [CrossRef]
23. Nasiri, M.; Mohammadi, R. Peak Current Limitation for Grid Side Inverter by Limited Active Power in PMSG-Based Wind Turbines During Different Grid Faults. *IEEE Trans. Sustain. Energy* **2017**, *8*, 3–12. [CrossRef]
24. Yaramasu, V.; Wu, B. *Model Predictive Control of Wind Energy Conversion Systems*; Wiley: New York, NY, USA, 2017; ISBN 9781118988589.
25. Sadiq, M.; Aragon, C.A.; Terriche, Y.; Ali, S.W.; Su, C.-L.; Buzna, Ľ.; Elsisi, M.; Lee, C.-H. Continuous-Control-Set Model Predictive Control for Three-Level DC–DC Converter with Unbalanced Loads in Bipolar Electric Vehicle Charging Stations. *Mathematics* **2022**, *10*, 3444. [CrossRef]
26. Azab, M. A Finite Control Set Model Predictive Control Scheme for Single-Phase Grid-Connected Inverters. *Renew. Sustain. Energy Rev.* **2021**, *135*, 110131. [CrossRef]
27. Babaghorbani, B.; Beheshti, M.T.; Talebi, H.A. A Lyapunov-Based Model Predictive Control Strategy in a Permanent Magnet Synchronous Generator Wind Turbine. *Int. J. Electr. Power Energy Syst.* **2021**, *130*, 106972. [CrossRef]
28. Kou, P.; Liang, D.; Li, J.; Gao, L.; Ze, Q. Finite-Control-Set Model Predictive Control for DFIG Wind Turbines. *IEEE Trans. Autom. Sci. Eng.* **2018**, *15*, 1004–1013. [CrossRef]
29. Caseiro, L.M.A.; Mendes, A.M.S.; Cruz, S.M.A. Dynamically Weighted Optimal Switching Vector Model Predictive Control of Power Converters. *IEEE Trans. Ind. Electron.* **2019**, *66*, 1235–1245. [CrossRef]

30. Li, X.; Zhang, H.; Shadmand, M.B.; Balog, R.S. Model Predictive Control of a Voltage-Source Inverter with Seamless Transition between Islanded and Grid-Connected Operations. *IEEE Trans. Ind. Electron.* **2017**, *64*, 7906–7918. [CrossRef]
31. Thapa, K.B.; Jayasawal, K. Pitch Control Scheme for Rapid Active Power Control of a PMSG-Based Wind Power Plant. *IEEE Trans. Ind. Appl.* **2020**, *56*, 6756–6766. [CrossRef]
32. Rahimi, M. Mathematical Modeling, Dynamic Response Analysis, and Control of PMSG-Based Wind Turbines Operating with an Alternative Control Structure in Power Control Mode. *Int. Trans. Electr. Energy Syst.* **2017**, *27*, e2423. [CrossRef]
33. Prior, G.; Krstic, M. A Control Lyapunov Approach to Finite Control Set Model Predictive Control for Permanent Magnet Synchronous Motors. *J. Dyn. Syst. Meas. Control. Trans. ASME* **2015**, *137*, 011001. [CrossRef]
34. Xia, C.; Liu, T.; Shi, T.; Song, Z. A Simplified Finite-Control-Set Model-Predictive Control for Power Converters. *IEEE Trans. Ind. Inform.* **2014**, *10*, 991–1002. [CrossRef]
35. Grid Converters for Photovoltaic and Wind Power Systems | IEEE EBooks | IEEE Xplore. Available online: https://ieeexplore.ieee.org/book/5732788 (accessed on 19 December 2021).
36. Alepuz, S.; Calle, A.; Busquets-Monge, S.; Kouro, S.; Wu, B. Use of Stored Energy in PMSG Rotor Inertia for Low-Voltage Ride-through in Back-to-Back NPC Converter-Based Wind Power Systems. *IEEE Trans. Ind. Electron.* **2013**, *60*, 1787–1796. [CrossRef]
37. Amer Saeed, M.; Mehroz Khan, H.; Ashraf, A.; Aftab Qureshi, S. Analyzing Effectiveness of LVRT Techniques for DFIG Wind Turbine System and Implementation of Hybrid Combination with Control Schemes. *Renew. Sustain. Energy Rev.* **2018**, *81*, 2487–2501. [CrossRef]
38. Talha, M.; Raihan, S.R.S.; Rahim, N.A. PV Inverter with Decoupled Active and Reactive Power Control to Mitigate Grid Faults. *Renew. Energy* **2020**, *162*, 877–892. [CrossRef]
39. Dai, J.; Xu, D.; Wu, B.; Zargari, N.R. Unified DC-Link Current Control for Low-Voltage Ride-through in Current-Source-Converter-Based Wind Energy Conversion Systems. *IEEE Trans. Power Electron.* **2010**, *26*, 288–297.
40. Barros, L.S.; Barros, C.M.V. An Internal Model Control for Enhanced Grid-Connection of Direct-Driven PMSG-Based Wind Generators. *Electr. Power Syst. Res.* **2017**, *151*, 440–450. [CrossRef]